Study on the design and structural optimization of excitation blocks for vibrators

Li Hong[1], Kewen Tian[2], Qiang Zhang[3], Ning Chen[4], Yize Liu[5]
[1, 2, 3, 4, 5]College of Information and Control Engineering, University of Emergency Management, Sanhe, 065201, People's Republic of China
[1, 3]Key Laboratory of Brain-Computer Interface Technology Application of the Ministry of Emergency Management, Sanhe, 065201, People's Republic of China
[1, 3]Langfang Key Laboratory of Accurately-Controlled Active Seismic Source, Sanhe, 065201, People's Republic of China
[3]Corresponding author
E-mail: [1]*cidphongli@163.com*, [2]*cidptiankewen@163.com*, [3]*zhangqiang@cidp.edu.cn*, [4]*cidpchenning@163.com*, [5]*saqrliuyize@163.com*

Received 16 October 2025; accepted 12 February 2026; published online 5 March 2026
DOI https://doi.org/10.21595/jve.2026.25596

Abstract. The performance of vibrator-based seismic sources is fundamentally constrained by the trade-off between excitation force and motor driving power. To address this challenge, a physics-informed framework for the parametric modeling and multi-objective optimization of annular-sector eccentric blocks is proposed. Firstly, a unified geometric model is established to derive closed-form expressions for mass properties, which are then integrated into a coupled electromechanical dynamic model to link geometric configurations directly with force output and power demand. To enhance computational efficiency, an Extreme-Frequency Substitution Strategy (EFSS) is introduced to reformulate the complex full-band dynamic optimization into a simplified static problem. The primary novelty of this work is the integration of physics-based geometric modeling, electromechanical dynamics, and extreme-frequency optimization within a single analytical framework. Sobol global sensitivity analysis reveals that the outer and inner radii are the dominant design drivers, while thickness and sector angle influence performance primarily through higher-order interactions. Using the NSGA-II algorithm, an optimized design is obtained that achieves a 10.52 % reduction in average peak driving power, a 35.26 % reduction in mass, and a 56.36 % reduction in the moment of inertia, while maintaining the required excitation force. This framework provides a rigorous and energy-efficient methodology for the design of next-generation controlled seismic vibrators.

Keywords: eccentric block, sensitivity analysis, NSGA-II, energy efficiency, vibrators.

Nomenclature

EFSS	Extreme-Frequency Substitution Strategy
NSGA-II	Non-dominated Sorting Genetic Algorithm II
CNC	Computer Numerical Control
LHS	Latin Hypercube Sampling
KDE	Kernel density estimation
FEA	Finite element analysis
$F(t)$	Excitation force of a single block
F_y	Resultant peak vertical excitation force of the vibrator
m, e	Eccentric mass and eccentricity
$\theta(t)$, ω	Angular position and angular velocity
$\mathbf{e}_x$, $\mathbf{e}_y$	Eccentricity components
ϕ, β	Central angle and half-central angle
R, r	Outer and inner radii of the annular sector
h, ρ	Thickness and material density of the eccentric block

P, T_{total}	Driving power and total torque
T_α, T_d, T_g	Inertial, damping, and gravitational torques
J	Eccentric mass moment of inertia
N_{rated}	Rated rotational speed
$P_{\min}, P_{rated}$	Minimum and rated power limits
$Var(Y)$	Total variance
S_1, S_T	First-order sensitivity index and total-order sensitivity index

1. Introduction

In recent decades, the increasing demand for shallow subsurface exploration and high-resolution dynamic monitoring of underground structures has driven the rapid advancement of vibrator-based seismic exploration [1], [2]. By artificially synthesizing controlled seismic waves, these systems have become indispensable tools for energy prospecting, geological investigation, and engineering diagnostics. Unlike conventional impulsive sources such as explosives and air guns [3], [4], vibrators operate on the principle of centrifugal force induced by rotating eccentric masses. Specifically, two eccentric blocks rotate synchronously in opposite directions to produce unidirectional vertical excitation, while a servo motor ensures precise control of rotational speed and phase. This configuration enables the injection of vertically polarized, periodic seismic waves into the ground with high stability and controllability [5], [6]. While controlled vibrators offer significant advantages in cost-effectiveness, their operational efficacy is governed by the intrinsic geometry and dynamic characteristics of the exciter. Consequently, a rigorous, physics-driven optimization of the exciter's geometry is indispensable for bridging the gap between theoretical efficiency and high-fidelity signal generation [7], [8]. The systematic design framework presented herein provides a theoretically sound and engineering-oriented methodology for the development of next-generation, lightweight, and high-efficiency seismic vibrators.

Despite the inherent advantages of vibrator-based seismic sources, their performance remains constrained by structural, dynamic, and control-related limitations. These challenges have catalyzed substantial research into enhancing mechanical architecture, energy transmission efficiency, and control accuracy. Field monitoring and experimental investigations have confirmed that optimizing base structures and vibrator-ground coupling effectively improves exploration depth and signal fidelity [9, 10]. Huang et al. [11, 12] demonstrated that geometric refinements and mass redistribution of the exciter can augment vibration amplitude while reducing phase error and high-frequency attenuation. From a system dynamics perspective, Zhang et al. [13] elucidated that judiciously tuning damping and dynamic parameters can significantly enhance energy transmission efficiency, highlighting the critical role of dynamic loss mechanisms. Similarly, Li et al. [14] and Peng et al. [15] revealed that mass, stiffness, and contact area are pivotal to energy transfer, providing valuable guidance for optimizing coupling conditions. Parallel developments in driving and control systems – such as active mass dampers [16], disturbance-compensation controllers [17], and linear synchronous motors [18] – have markedly improved excitation stability and anti-interference capability. Concurrently, advances in signal processing, including waveform reconstruction and phase recognition, have enhanced the time-frequency resolution of recorded signals [6, 19]. Improvements in bearing design and eccentric structural configurations have also contributed to superior dynamic balance and energy utilization [20-22]. For diverse scenarios, multi-parameter joint optimization frameworks have been proposed to improve the signal-to-noise ratio and exploration efficiency [23-25]. Moreover, trajectory planning and smooth time-optimal control methods in CNC systems [26, 27] offer conceptual insights for designing excitation profiles that achieve coordinated motion – principles applicable to vibrator control strategies. Nevertheless, a research gap persists in quantitatively understanding how the generalized morphology of the exciter governs the fundamental trade-off between excitation output and driving power under coupled force–power constraints.

Despite extensive efforts to enhance vibrator performance, most existing studies implicitly regard exciter geometry as a fixed or rigidly constrained parameter, typically limited to conventional cylindrical or semi-cylindrical forms. Such geometric simplifications restrict the degrees of freedom in mass redistribution and, more critically, obscure the intrinsic coupling between excitation force generation and driving power demand [17]. While multi-objective optimization has been applied to specific exciter configurations, these approaches are generally confined to predefined, geometry-restricted parameter spaces. Consequently, they fail to capture how geometric morphology fundamentally governs the force–power trade-off. As a result, the physical limits of eccentric exciter performance remain poorly quantified, hindering the development of versatile, geometry-aware optimization frameworks.

To address these limitations, this study proposes a generalized parametric modeling and multi-objective optimization framework for annular-sector eccentric excitation blocks. Unlike existing studies that rely on case-specific geometries or empirical tuning, we first establish a unified geometric representation to describe a broad class of sector configurations. This approach enables closed-form analytical expressions for mass, eccentricity, and moment of inertia. On this basis, a coupled electromechanical dynamic model is developed to explicitly quantify the nonlinear interplay between geometric parameters, excitation force, and driving power across the operating frequency range. To reduce the computational burden of full-band optimization, an Extreme-Frequency Substitution Strategy (EFSS) is introduced, transforming the wide-band dynamic problem into an efficient static multi-objective formulation. Furthermore, global sensitivity analysis and NSGA-II optimization are integrated to reveal the governing geometric mechanisms and to identify optimal design solutions. The proposed framework provides a physics-informed and reproducible pathway for achieving lightweight, energy-efficient exciters, offering practical guidance for the development of next-generation controlled seismic vibrators.

2. Modeling and working principle

The seismic vibrator is a high-precision source system operating on the principle of mechanical rotation, as illustrated in Fig. 1. Its functional core involves the precise control of two identical eccentric masses, which undergo synchronized counter-rotation driven by servo motors. This configuration generates a periodic excitation force orthogonal to the ground, thereby launching directional seismic waves into the subsurface.

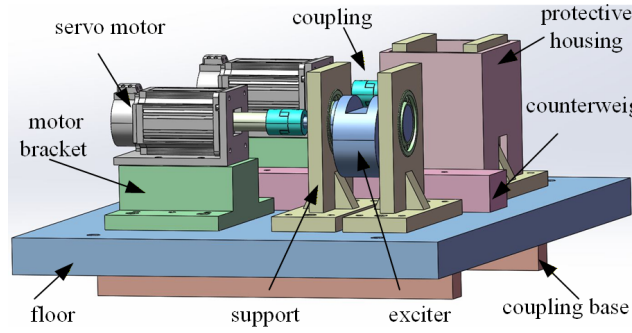

Fig. 1. Schematic diagram of the vibrator's structure and operating principle

During operation, the mass (m) of each eccentric block remains constant. By controlling the angular position $\theta(t)$ and angular velocity (ω) of the servo motor, the system produces highly repeatable and controllable vibration signals. When coupled to the ground, the system induces forced vibrations through baseplate-ground interaction, ensuring efficient energy transfer and high-fidelity excitation.

2.1. Dynamic modeling of the excitation force

The excitation force arises from the centrifugal forces generated by the rotating eccentric masses. For a single eccentric block with mass m and eccentricity e, rotating at a constant angular velocity ω, the instantaneous centrifugal force vector can be expressed as:

$$F(t) = me\omega^2\left[\sin\theta\,(t)\mathbf{e}_x + \cos\theta\,(t)\mathbf{e}_y\right], \tag{1}$$

where $\theta(t)$ is the instantaneous angular position and $\mathbf{e}_x$ are $\mathbf{e}_y$ unit vectors in the horizontal and vertical directions, respectively.

In the proposed dual-eccentric configuration, two identical eccentric blocks rotate synchronously at the same angular velocity ω in a symmetric, counter-rotating manner. Under this condition, the horizontal components of the centrifugal forces are equal in magnitude but opposite in direction, thereby achieving complete self-cancellation in the horizontal plane. In contrast, the vertical components are constructively superimposed in phase, producing a purely unidirectional periodic excitation force, as illustrated in Fig. 2.

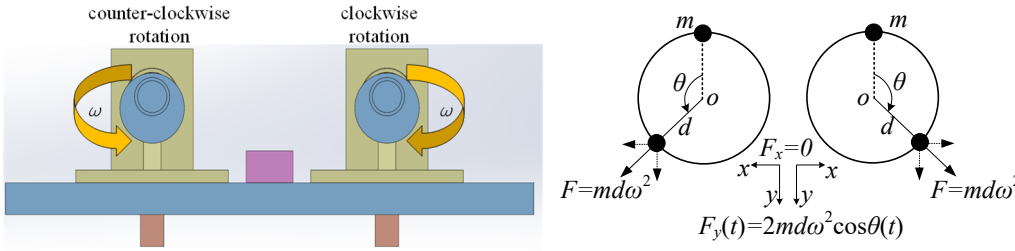

a) Schematic of the internal working principle

b) Vector synthesis of the centrifugal force components

Fig. 2. Working principle and mechanical model of the exciter

Based on this vector synthesis mechanism, the resultant peak vertical excitation force, F_y, produced by the entire vibrator system can be derived in the following closed form:

$$F_y = 2me\omega^2. \tag{2}$$

Eq. (2) provides the analytical foundation for evaluating the excitation force throughout this study. It explicitly demonstrates that the excitation magnitude is uniquely governed by the mass distribution (m and e) and the angular velocity (ω). Since the operating frequency is dictated by motor and system limitations, the excitation force can be effectively optimized through the geometric design of the eccentric blocks. This explicit relationship serves as the physical basis for the parametric modeling, sensitivity analysis, and multi-objective optimization discussed in the subsequent sections.

2.2. Parametric modeling of mass properties

To facilitate systematic sensitivity analysis and multi-objective optimization, a closed-form, parametric representation of the eccentric block's mass properties is essential. Among conventional geometries – such as semi-cylindrical, circular, and annular forms – the annular-sector configuration offers the highest degree of geometric flexibility. By modulating its central angle, this geometry can seamlessly represent semi-cylindrical configurations ($\phi = 180°$) or approximate annular structures within specific parameter limits.

Accordingly, a unified sector-based geometric model is adopted in this study, as illustrated in Fig. 3. The eccentric block comprises a solid cylindrical core of radius r and a surrounding annular

sector with outer radius R, thickness h, and a total aperture angle $\phi = 2\beta$. Let ρ denote the material density; the total mass of the eccentric block is then expressed as:

$$m = \rho h \pi \left(r^2 + \frac{\beta}{180}(R^2 - r^2) \right), \tag{3}$$

where β is the half-central angle expressed in degrees.

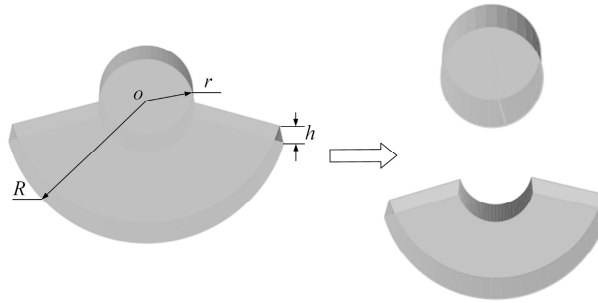

Fig. 3. Geometric configuration and design parameters of the annular-sector eccentric block

The eccentricity e is defined as the distance between the composite centroid of the block and the rotation center. Due to its rotational symmetry, the cylindrical core yields zero net contribution to the overall eccentricity. Consequently, the resultant eccentricity of the entire eccentric block is derived as:

$$e = \frac{120}{\pi} \cdot \frac{(R^3 - r^3)\sin\beta}{\beta R^2 + (180 - \beta) r^2}, \tag{4}$$

where β is the half-central angle of the sector. In the analytical formulations, β is expressed in degrees when used as a standalone variable, while its radian equivalent is adopted within trigonometric functions (e.g., $\sin\beta$) to ensure numerical correctness.

By substituting Eqs. (3) and (4) into Eq. (2), the excitation force can be explicitly expressed as a function of the geometric design variables (R, r, h, β). This closed-form formulation enables rapid and robust evaluation of dynamic performance, facilitating efficient large-scale parametric studies and multi-objective optimization.

2.3. Driving power model

The driving power P is a critical metric for motor specification, thermal safety, and overall system efficiency. It is determined by the total driving torque required to overcome inertial resistance, viscous damping, and gravitational effects during rotation:

$$P = T_{total}\omega, \tag{5}$$

where the total driving torque T_{total} is decomposed as:

$$T_{total} = T_\alpha + T_d + T_g. \tag{6}$$

The inertial torque T_α required to accelerate the eccentric block is defined by:

$$T_\alpha = J\alpha, \tag{7}$$

where J is the mass moment of inertia and α denotes the angular acceleration. Based on the annular-sector geometry illustrated in Fig. 3, the total moment of inertia is derived as:

$$J = \frac{\pi h \rho}{360}(\beta R^4 + (180 - \beta) r^4). \tag{8}$$

The damping torque T_d accounts for viscous losses in bearings and transmission components and is modeled as:

$$T_d = d\omega, \tag{9}$$

where d represents the viscous damping coefficient.

The gravitational torque T_g induced by the eccentric mass is expressed as:

$$T_g = mge \sin\theta\,(t), \tag{10}$$

where g denotes gravitational acceleration.

For conservative motor sizing and the comparative evaluation of different geometries, the peak driving power during the start-up phase is estimated by evaluating Eq. (5) under the worst-case orientation, which corresponds to the maximum gravitational torque. This approach ensures that the selected motor can reliably initiate rotation from a standstill under maximal load conditions.

2.4. Modeling assumptions

To balance analytical tractability with physical fidelity, the following assumptions are systematically adopted throughout the modeling, sensitivity analysis, and optimization procedures. All subsequent numerical simulations strictly adhere to this established framework:

(1) Gravitational Loading: The gravitational torque is evaluated at its worst-case orientation to ensure a robust estimation of the maximum power demand.

(2) Rigid-Body Dynamics: The entire system is modeled as a strictly rigid-body system; consequently, the elastic deformation of the shafts, and supporting structures is omitted [20].

(3) Viscous Damping: Rotational resistance is represented by a linear viscous damping model with a constant coefficient, thereby aggregating the complex frictional losses in the bearings and transmission components [28].

(4) Kinematic Characteristics: During the start-up phase, a constant angular acceleration is assumed, facilitating a conservative estimation of the peak driving power [29].

(5) Coupling Boundary Conditions: Explicit ground-structure coupling effects are excluded from this study; instead, the analysis focuses exclusively on the intrinsic excitation generation and the corresponding motor-side power requirements [17].

Within the scope of these assumptions, the proposed analytical framework provides a consistent, transparent, and computationally efficient foundation for the sensitivity analysis, multi-objective optimization, and robustness evaluation presented in the subsequent sections.

3. Multi-objective optimization problem formulation

The effective formulation of a multi-objective optimization problem necessitates a clear and physically interpretable definition of the objective functions, design variables, and operational constraints. This section establishes a rigorous optimization framework grounded in the analytical models derived in Section 2, thereby ensuring both mathematical consistency and engineering relevance.

3.1. Optimization objectives and the extreme-frequency substitution strategy

This study aims to simultaneously address two inherently conflicting objectives: maximizing the total excitation force F_y and minimizing the operational driving power P, subject to prescribed structural and operational constraints.

However, a direct formulation of this multi-objective problem across the entire operational bandwidth, $\omega \in [\omega_{min}, \omega_{max}]$, presents substantial computational and theoretical challenges. First, evaluating system performance at every discrete frequency point would impose a prohibitive computational burden within iterative evolutionary frameworks, such as NSGA-II. Second, aggregating frequency-dependent metrics via weighting factors often lacks rigorous physical justification, which may bias the optimization toward solutions that are mathematically optimal but physically inconsistent.

These impediments can be resolved by exploiting the intrinsic monotonicity of the centrifugal excitation mechanism. Based on the analytical models established in Section 2, and as evidenced by the normalized results in Fig. 4, both the total excitation force F_y and the driving power P increase monotonically with the angular frequency ω for any fixed geometric configuration.

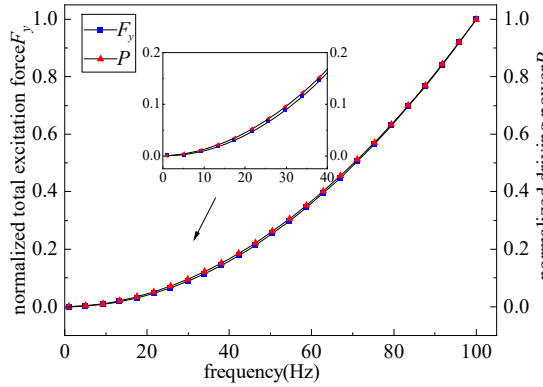

Fig. 4. Normalized variations of total excitation force and driving power with angular frequency

This monotonic relationship permits a rigorous dimensionality reduction of the original dynamic optimization problem. Specifically, maximizing the total excitation force over the entire operating bandwidth is functionally equivalent to maximizing F_y at the lowest working frequency (ω_{min}), while minimizing the overall power demand is effectively addressed by minimizing the driving power P at the highest frequency (ω_{max}).

Consequently, an Extreme-Frequency Substitution Strategy (EFSS) is introduced, whereby the original frequency-dependent problem is reformulated as a static optimization task evaluated at these two spectral extremes. The resulting objective functions are defined as:

$$\text{Maximize} \quad \left[F_y(\omega_{min}), -P(\omega_{max})\right]^T, \tag{11}$$

where $F_y(\omega_{min})$ represents the total excitation force at the lowest working frequency, and $P(\omega_{max})$ represents the driving power at the highest working frequency. This reformulation preserves the physical essence of the original problem while significantly enhancing computational efficiency and numerical robustness.

3.2. Design variables and bounding constraints

The design variables are derived directly from the generalized parametric model presented in Section 2.2 and are defined as:

$$X = \{R, r, h, \beta\}, \tag{12}$$

where, R denotes the outer radius (m), r is the inner radius (m), h represents the axial thickness (m), and β is the half-central angle (degrees).

To ensure manufacturability and assembly feasibility, each design variable is strictly constrained within a physically admissible range dictated by engineering practice and spatial limitations. These boundary constraints ensure that the resulting exciter configuration remains within the operational envelope of the seismic vibrator. The corresponding parameter bounds are summarized in Table 1.

Table 1. Design parameter range

Design variable	R	r	h	β
Maximum value	0.07 m	0.065 m	0.2 m	89°
Minimum value	0.01 m	0.01 m	0.01 m	5°

3.3. Dynamic and geometric constraints

To ensure physical realizability, operational safety, and engineering relevance, the following design constraints are imposed:

Geometric Feasibility Constraints: To maintain the structural integrity of the annular sector, the outer radius R must strictly exceed the inner radius r. A safety margin (δ_{safe}) is introduced to account for structural stability and manufacturing tolerances:

$$r \leq R - \delta_{safe}, \tag{13}$$

where $\delta_{safe} = 0.005$ is set to a representative engineering value.

Operational Constraints: The operating frequency is constrained within 5 Hz $\leq \omega \leq$ 25 Hz, which defines the effective working bandwidth. Consequently, the associated angular velocity ω must satisfy:

$$\omega_{min} \leq \omega \leq \omega_{max} = \frac{2\pi N_{rated}}{60}, \tag{14}$$

where N_{rated} denotes the rated speed of the servo motor (rpm).

Power Constraints: To preclude motor overloading, the driving power $P(\omega_{max})$ a at the peak frequency must not exceed the motor's rated power P_{rated}. Furthermore, to ensure the optimization results maintain practical utility and do not converge to trivial low-power solutions, a lower limit P_{min} is established. The driving power constraint is thus formulated as:

$$P(\omega_{max}) \in [P_{min}, P_{rated}]. \tag{15}$$

For the numerical evaluation of dynamic performance indices, specific parameter values are assigned in accordance with the physical assumptions in Section 2.4. The angular acceleration during the start-up phase is defined as a constant $\alpha = 25\pi$ rad/s^2, representing a conservative ramp-up profile within the motor's dynamic capabilities. Rotational losses are parameterized by an equivalent viscous damping coefficient $d =$ 0.005 N·m·s/rad, which is adopted as a representative value for the considered operating range.

With the objective functions, design variables, and constraints fully defined, the multi-objective optimization problem is now well-posed. All Pareto-optimal solutions obtained in the subsequent analysis are guaranteed to reside within a physically admissible and practically feasible design manifold.

4. Sensitivity analysis

Sensitivity analysis provides a rigorous statistical framework for quantifying the relative impact of design parameters on system-level performance metrics [30]. In this study, the Sobol global sensitivity analysis method is employed to systematically evaluate the individual and collective contributions of the four geometric design variables – outer radius R, inner radius r, thickness h, and half-central angle β – to the performance indices, namely the total excitation force (F_y) and driving power (P). In addition to identifying dominant parameters, this method also captures nonlinear coupling effects among variables. The resulting sensitivity indices offer profound physical insights into the parameter-to-performance mappings, providing a theoretical foundation for variable selection and prioritization in the subsequent multi-objective optimization.

4.1. Methodology and workflow

The Sobol method is a variance-based global sensitivity analysis technique uniquely suited for models exhibiting strong nonlinearity and complex multi-variable coupling. The core principle involves decomposing the total variance ($Var(Y)$) of the model output ($Y = f(X)$) into fractional components attributable to individual input variables and their high-order interactions.

The total variance of the output Y can be decomposed into a sum of variances contributed by each input variable X_i and their interaction terms:

$$\mathrm{Var}(Y) = \sum_i \mathrm{Var}(E[Y|X_i]) + \sum_{i<j} \mathrm{Var}\left(E\left[Y\middle|X_i, X_j\right]\right) + \cdots + \mathrm{Var}(E[Y|X_1, \cdots, X_k]). \tag{16}$$

First-order sensitivity index (S_1): This index quantifies the principal effect of an individual variable X_i on the output variance when considered independently. It is defined as the ratio of the conditional variance to the total variance:

$$S_1 = \frac{Var(E[Y|X_i])}{Var(Y)}. \tag{17}$$

Total-order sensitivity index (S_T): This index measures the aggregate influence of X_i, encompassing both its direct contribution and all higher-order interactions with other variables:

$$S_T = 1 - \frac{\mathrm{Var}(E[Y|X_{\sim i}])}{\mathrm{Var}(Y)}, \tag{18}$$

where $X_{\sim i}$ denotes the set of all input variables excluding X_i. A significant divergence between S_T and S_1 serves as a definitive diagnostic of strong nonlinear coupling effects.

To ensure uniform coverage of the high-dimensional design space, Saltelli's extension of the Sobol quasi-random sequence was employed. A fixed random seed was utilized to ensure numerical reproducibility. The base sample size N was progressively increased from 504 to 9,500, corresponding to a final total of 9,500 model evaluations $(2k + 2) \times N$, $k = 4$. All samples were evaluated using the direct analytical models derived in Section 2, thereby eliminating surrogate-induced errors and preserving the physical fidelity of the nonlinear dynamic behavior.

The convergence behavior of the Sobol sensitivity indices is illustrated in Figs. 5 and 6. For the dominant parameters R and r, both first-order and total-order indices rapidly converge to stable plateaus, indicating robust independent contributions. In contrast, the indices associated with thickness h and angle β exhibit moderate fluctuations at lower evaluation counts, suggesting that their influence is manifested primarily through interdependent interactions rather than isolated effects.

Once the number of model evaluations exceeds approximately 9,500, all sensitivity indices

exhibit negligible variation with further increases in sample size, indicating statistical convergence. The quasi-random nature of the Sobol sequence further improves numerical stability compared with conventional Monte Carlo sampling. This convergence threshold serves as the criterion for statistical adequacy, thereby ensuring the reliability of the subsequent sensitivity ranking.

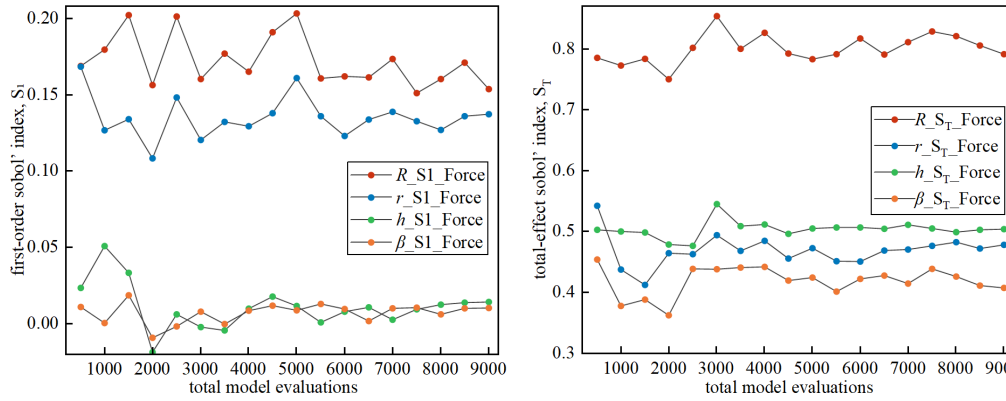

a) First-order indices. b) Total-order indices

Fig. 5. Sobol sensitivity indices for total excitation force

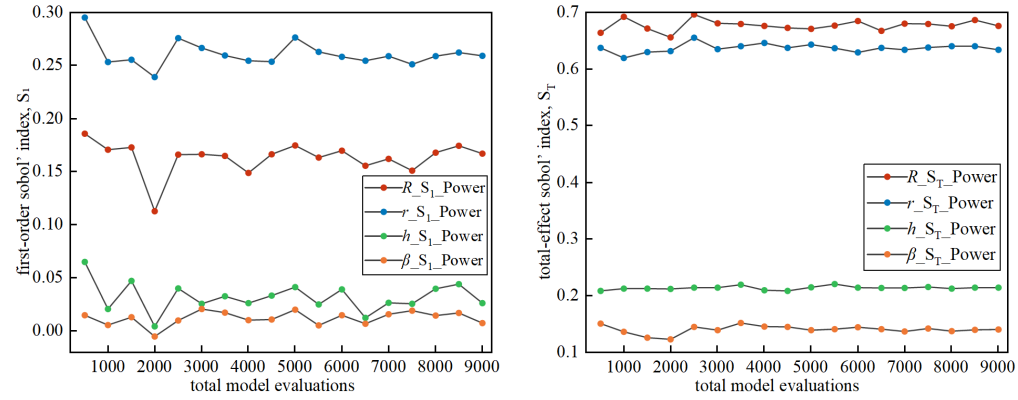

a) First-order indices. b) Total-order indices

Fig. 6. Sobol sensitivity indices for driving power

4.2. Results of sensitivity analysis

The converged Sobol indices summarized in Fig. 7 reveal that the outer radius R is the most influential parameter governing both the total excitation force and driving power. This is underscored by its dominant first-order and total-order sensitivity indices, which account for the majority of the output variance. The inner radius r also exerts a substantial impact, though its influence is channeled primarily through strong interaction effects with R. In contrast, the thickness h and half-central angle β exhibit minimal independent contributions ($S_1 \approx 0$). Nevertheless, their non-zero total-order indices suggest a latent influence through higher-order nonlinear coupling, particularly when interacting with the dominant radial parameters. The persistent condition $S_T > S_1$ across all variables quantitatively confirms that the vibrator's dynamic response is governed by intricate multivariable interplay rather than separable, linear parameter effects.

These findings have direct strategic implications for structural optimization. The pronounced

dominance of R and r identifies them as the primary design drivers that must be prioritized. Furthermore, the significant interaction effects validate the necessity of a global multi-objective optimization framework, precluding the effectiveness of sequential or single-parameter tuning strategies. Concurrently, the non-trivial coupling involving h and β underscores that seemingly secondary geometric features can exert a meaningful leverage on system performance through synergistic interaction pathways. Consequently, this sensitivity analysis offers rigorous theoretical justification for the multi-objective optimization strategy detailed in the subsequent section.

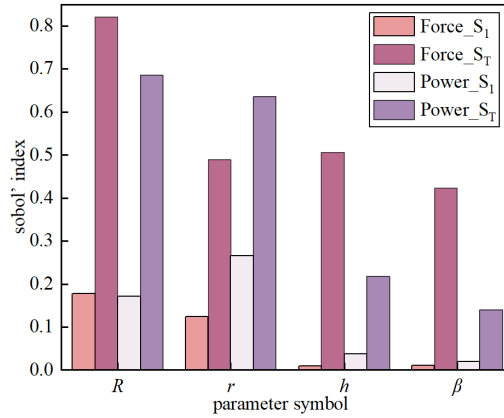

Fig. 7. First-order and total-order Sobol sensitivity indices for total excitation force and driving power

5. Multi-objective optimization and analysis of results

This section presents a comprehensive global multi-objective optimization study of the proposed excitation block geometry, focusing on the trade-off between the total excitation force and the driving power.

5.1. Optimization algorithm and performance evaluation

The Non-dominated Sorting Genetic Algorithm II (NSGA-II) was employed to solve the coupled multi-objective optimization problem, balancing the maximization of total excitation force against the minimization of driving power. NSGA-II was selected for its proven efficacy in navigating nonlinear, non-convex Pareto fronts absent gradient information – a characteristic particularly advantageous for complex systems governed by nonlinear geometric-dynamic coupling [31], [32].

The overall optimization workflow is illustrated in Fig. 8.

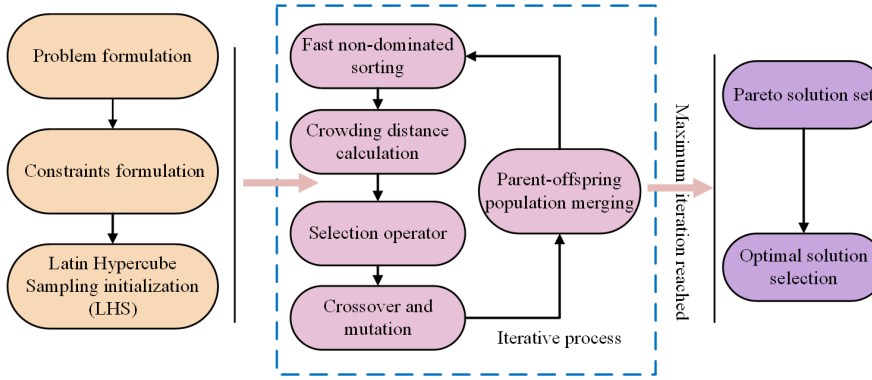

Fig. 8. NSGA-II algorithm flowchart

To ensure numerical rigor and reproducibility, all stochastic operations were controlled using a fixed random seed (seed = 42). The initial population was generated via Latin Hypercube Sampling (LHS) to guarantee uniform exploration of the four-dimensional design space (R, r, h, β). All objective functions were evaluated directly using the closed-form analytical models derived in Section 2. Crucially, no surrogate or response surface approximations were introduced, thereby retaining the full physical fidelity of the model throughout the optimization process.

A population size of 1000 individuals evolved over 100 generations was adopted, culminating in 100,000 function evaluations. Simulated Binary Crossover (SBX) and polynomial mutation were implemented with probabilities of 0.9 and 0.1, respectively. Constraint handling was executed through feasibility-based selection during fitness evaluation, and algorithmic convergence was quantitatively verified by the stabilization of the Pareto front across successive generations. The detailed hyperparameter configuration for the NSGA-II is summarized in Table 2.

Table 2. NSGA-II parameter settings

Parameter	Symbol	Value
Population size	pop_size	1000
Generations	ngen	100
Crossover probability	cxpd	0.9
Mutation probability	mutpd	0.1
Crossover index	cx_eta	5.0
Mutation index	mut_eta	5.0

5.2. Optimization results

The Pareto-optimal front obtained via NSGA-II is presented in Fig. 9. The smooth and continuous topology of the front clearly elucidates the intrinsic trade-off between excitation capability and energy consumption, substantiating the premise that no single geometric configuration can simultaneously optimize both objectives.

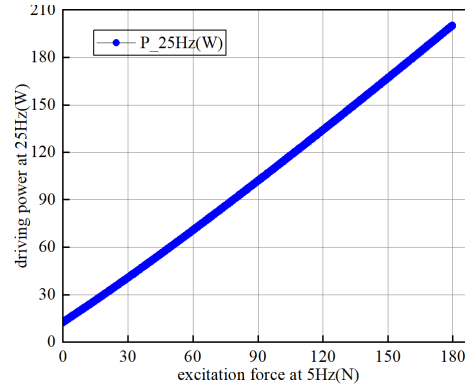

Fig. 9. Pareto optimal front

The distribution of Pareto-optimal solutions within the design variable space (Fig. 10) provides direct insight into the underlying governing mechanisms. The outer radius R spans nearly its entire feasible range along the Pareto front, which is fully congruent with its dominant influence on both objectives as identified by the Sobol sensitivity analysis. In contrast, the inner radius r consistently converges toward its minimum allowable value; this reflects a structural imperative to maximize the effective eccentric mass while eliminating dynamically inactive material. Furthermore, the thickness h also tends toward its upper bound in high-force solutions, underscoring its secondary but monotonic influence on the output.

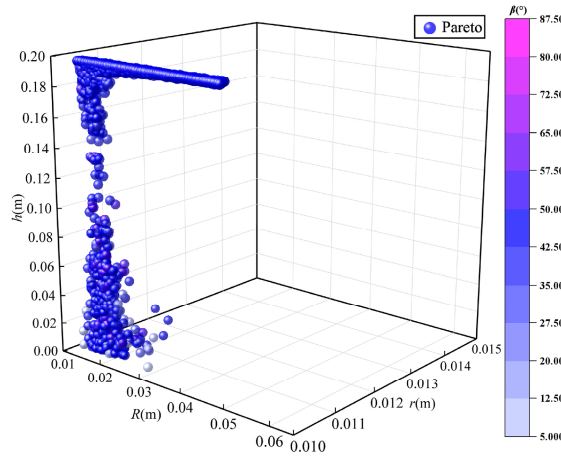

Fig. 10. Distribution of Pareto optimal solutions in the design variable space

A particularly compelling observation concerns the behavior of the half-central angle β. As shown by the frequency distribution in Fig. 11, the Pareto-optimal solutions do not saturate at the parameter bounds but instead cluster predominantly around an interior value of $\beta \approx 48°$. While eccentricity reaches its theoretical maximum at a slightly higher angle for the present geometry, further increases in β yield only diminishing marginal gains in eccentricity. Crucially, such increases induce a nearly linear growth in total mass and rotational inertia. Given that the driving power is inertia-dominated, this results in a disproportionate power penalty. Consequently, the optimization algorithm identifies an interior value of β that maximizes excitation efficiency rather than eccentricity alone.

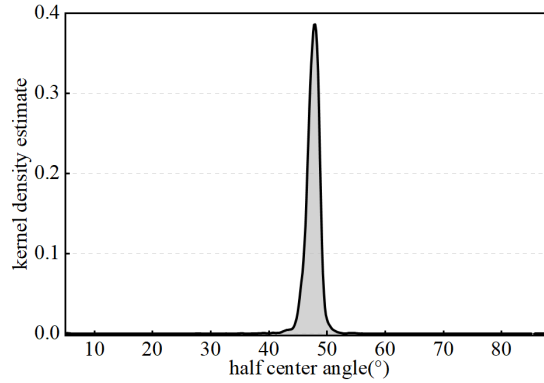

Fig. 11. Frequency distribution of the half-central angle (β) among Pareto-optimal solutions

Collectively, these distribution patterns demonstrate that the Pareto front emerges from complex nonlinear interactions among geometric parameters, rather than a mere combination of parameter extremes. The proposed multi-objective framework effectively leverages these interactions to identify physically meaningful and practically realizable designs that optimally balance excitation performance and energy efficiency.

5.3. Analysis of representative optimal solutions

To further elucidate the design trade-offs along the Pareto front, three representative configurations were selected for detailed comparison: (A) Maximum Excitation Force, (B) Balanced Compromise, and (C) Minimum Driving Power. The geometric parameters and

corresponding performance metrics for these cases are summarized in Table 3, with a comparative performance visualization provided in Fig. 12.

Table 3. Representative optimal solutions

Parameter	Outer radius R	Inner radius r	Thickness h	Half-central angle β	Total excitation force (25 Hz)	Driving power (25 Hz)
Case(A): Max. force	0.043 m	0.010 m	0.200 m	47.80 °	3003.93 N	133.98 W
Case(B): Compromise	0.03 m	0.010 m	0.200 m	48.20 °	1001.12 N	50.42 W
Case(C): Min. power	0.023 m	0.010 m	0.050 m	45.00 °	101.96 N	16.11 W

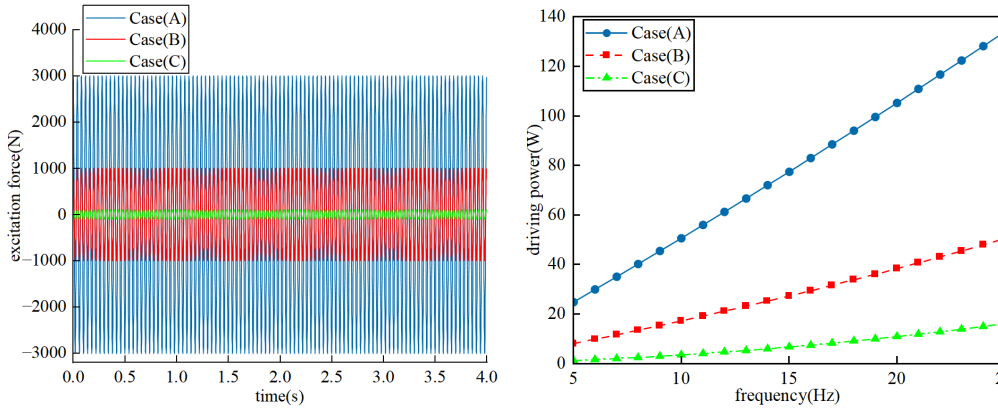

a) Total excitation force at 25 Hz b) Driving power at 25 Hz

Fig. 12. Performance comparison of the representative Pareto-optimal configurations

This compromise configuration represents the most practically viable and economically efficient design for standard exploration scenarios. Its selection underscores the effectiveness of the proposed optimization framework and reaffirms the physical consistency of the underlying analytical models. By reconciling the inherent conflict between excitation intensity and power demand, this design offers a robust technical foundation for the next generation of high-precision seismic exciters.

6. Validation of optimized vibrators design

To rigorously validate the effectiveness, robustness, and structural feasibility of the proposed multi-objective optimization framework, a multi-level verification study was conducted. First, a comparative dynamic simulation was performed between a conventional reference design and an optimized excitation-block configuration selected from the Pareto front obtained via the NSGA-II algorithm, with emphasis on excitation force generation and driving power over the full operational bandwidth (5-25 Hz). Subsequently, the robustness of the optimized design against inevitable manufacturing tolerances was quantified through Monte Carlo simulations and kernel density estimation (KDE). Finally, high-fidelity finite element analysis (FEA) was employed to verify the structural integrity and von Mises stress distribution of the optimized configuration under peak centrifugal loading.

6.1. Validation of inertial properties and wide-band driving power performance

The key structural parameters and calculated inertial properties for the conventional, optimized, and equivalent cylindrical configurations are summarized in Table 4.

Table 4. Comparison of key parameters between conventional and optimized designs

Design	Outer radius R	Inner radius r	Thickness h	Half-angle β	Eccentric mass m	Total moment of inertia I	Driving power at 25 Hz
Conventional design	0.03 m	0.02 m	0.13 m	50.3 °	1.73 Kg	5.5×10^{-4} Kg·m^2	33.07 W
Optimized design	0.024 m	0.010 m	0.2 m	47.8 °	1.12 Kg	2.4×10^{-4} Kg·m^2	29.98 W
Equivalent Cylinder	0.03 m	0	0.045 m	180 °	0.99 Kg	5.4×10^{-4} Kg·m^2	34.45 W

The structural comparison highlights a significant breakthrough achieved through the optimization process. The optimized design reduces the eccentric mass by 35.26 % (from 1.73 kg to 1.12 kg) and, even more remarkably, achieves a 56.36 % reduction in the total moment of inertia (from 5.5×10^{-4} to 2.4×10^{-4} kg·m^2). This pronounced decoupling between mass and rotational inertia confirms that the NSGA-II framework effectively leverages geometric degrees of freedom – specifically by minimizing the inner radius and redistributing material toward dynamically efficient regions – to attain superior inertial performance.

The comparison of simulated driving power over the entire operational bandwidth is presented in Fig. 13.

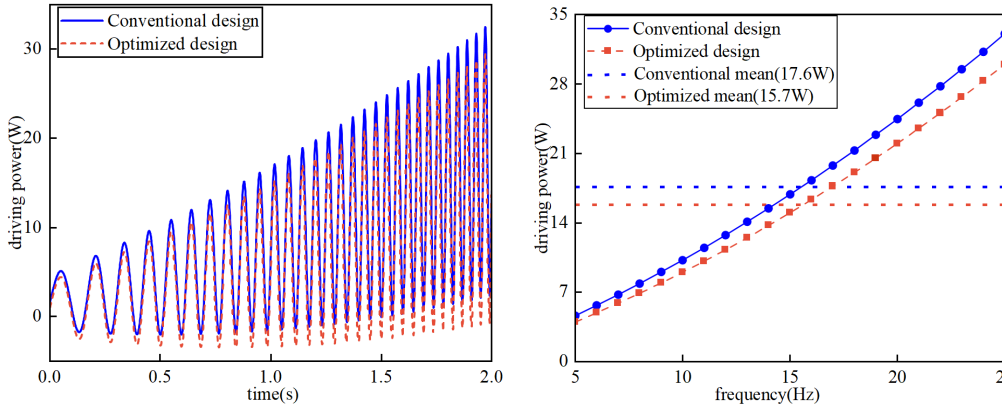

a) Simulated waveforms b) Maximum driving power versus frequency

Fig. 13. Comparative simulation results of the conventional and optimized designs

The results unambiguously demonstrate that the optimized configuration consistently outperforms the conventional design, requiring lower driving power across the entire frequency range. At the maximum frequency of 25 Hz, the conventional design consumes 33.07 W, whereas the optimized design requires only 29.98 W. When integrated over the full frequency spectrum, the optimized design achieves an average 10.52 % reduction in peak driving power. This indicates that the performance enhancement is not merely confined to discrete operating points but is inherently robust across the bandwidth. Notably, this substantial reduction in power demand is achieved without compromising the excitation force output, thereby vindicating the optimized geometry as a superior solution for balancing excitation capability with energy efficiency.

6.2. Robustness and tolerance analysis

To assess the sensitivity of the optimized geometric design to machining uncertainties, a stochastic analysis using Monte Carlo simulation with 10,000 random samples was performed. The linear dimensions (R, r, h) were perturbed within ± 0.2 mm, and the half-central angle β within ±0.5°, representing stringent yet typical CNC manufacturing tolerances.

Fig. 14 presents the kernel density estimation (KDE) for the total excitation force at 5 Hz and

the driving power at 25 Hz. Both distributions are conspicuously narrow and unimodal, indicating the superior robustness of the optimized design against aleatory manufacturing deviations.

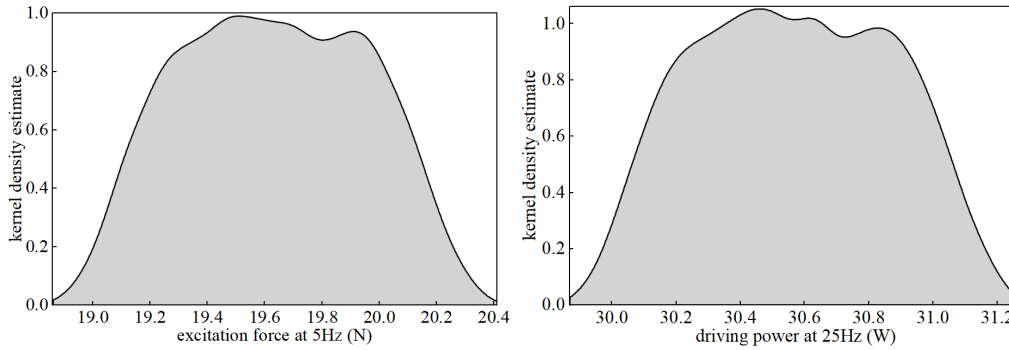

a) Kernel density estimate of the total excitation force at 5 Hz

b) Kernel density estimate of the driving power at 25 Hz

Fig. 14. Robustness analysis of the optimized eccentric block under manufacturing tolerances

Quantitatively, the total excitation force exhibits a coefficient of variation below 1 %, while the driving power shows a variation of less than 0.6 %. These results conclusively demonstrate that the optimized configuration maintains consistent dynamic performance even under realistic manufacturing variances. This vindicates the Pareto-optimal solution as being not only mathematically superior but also practically resilient and reliable for industrial production.

6.3. Finite element verification of structural feasibility

To validate the structural reliability of the optimized parameters identified in Section 6.1, a high-fidelity finite element analysis (FEA) was performed. Fig. 15 illustrates the von Mises equivalent stress and total deformation of the optimized annular-sector eccentric block under peak operational loads.

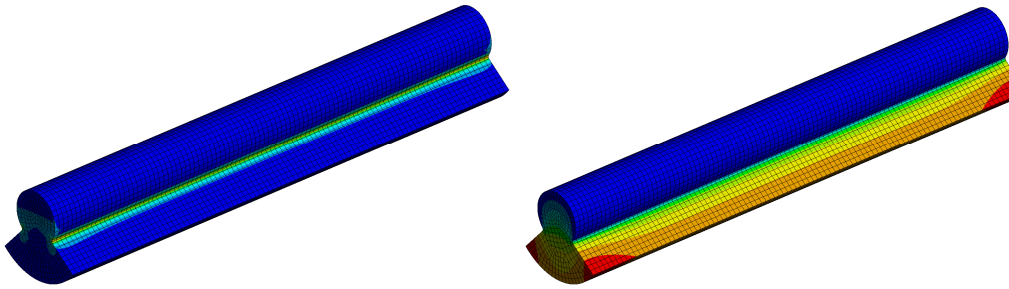

a) Von Mises stress distribution of the optimized eccentric exciter at $\omega = 157$ rad/s

b) Total deformation distribution of the optimized eccentric exciter at $\omega = 157$ rad/s

Fig. 15. Finite element results of the optimized eccentric exciter under the maximum rotational speed

As depicted in Fig. 15(a), the maximum von Mises stress is approximately 0.41 MPa. This value is several orders of magnitude below the yield strength of conventional structural steels, providing an extensive safety margin. The uniform stress gradient confirms that the optimized geometry effectively mitigates potential stress concentration during high-speed rotation. Correspondingly, the total deformation is numerically negligible, with a peak value of only 7.15×10^{-6} m (Fig. 15(b)). This combination of exceptional structural rigidity and minimal mechanical compliance ensures the dynamic stability of the centrifugal excitation force. These results conclusively verify that the optimized design fully satisfies the stringent structural

ISSN PRINT 1392-8716, ISSN ONLINE 2538-8460

reliability requirements necessitated by high-frequency seismic excitation applications.

7. Conclusions

This study establishes a physics-informed analytical and multi-objective optimization framework for annular-sector eccentric blocks in vibrator-based seismic sources, offering a unified analytical perspective compared to traditional empirical designs. By formulating closed-form relationships that directly link geometric parameters with the total excitation force and driving power, this framework provides a precise physical interpretation of the inherent force-power trade-off. To address the complexity of full-band dynamic optimization, an Extreme-Frequency Substitution Strategy (EFSS) was introduced to reduce the problem to an efficient static formulation without loss of physical fidelity. Global sensitivity analysis further revealed that while the outer and inner radii dominate system behavior, the thickness and half-central angle influence performance primarily through nonlinear coupling effects. Utilizing the NSGA-II algorithm, the optimization identified an optimal interior half-central angle ($\beta \approx 48°$) and produced a configuration that achieved a substantial 56.36 % reduction in the total moment of inertia, a 35.26 % reduction in mass, and a 10.52 % decrease in peak driving power, all while retaining full excitation capability. Finite element verification confirmed the engineering feasibility of these results, demonstrating that the proposed framework provides a rigorous, energy-efficient methodology for the design of next-generation controlled seismic vibrators.

Acknowledgements

This study was financially Funded by Science Research Project of Hebei Education Department (Grant No. QN2026101), the Fundamental Research Funds for the Central Universities (Grant No. ZY20250203) and the Science and Technology Innovation Program for Postgraduate students in IDP subsidized by Fundamental Research Funds for the Central Universities (Grant No. ZY20260315).

Data availability

The datasets generated during and/or analyzed during the current study are available from the corresponding author on reasonable request.

Author contributions

Li Hong: writing-original draft, methodology, conceptualization. Kewen Tian: investigation, formal analysis, software, visualization. Qiang Zhang: writing-review and editing, methodology, funding acquisition, supervision, data curation. Ning Chen: software, conceptualization. Yize Liu: investigation.

Conflict of interest

The authors declare that they have no conflict of interest.

References

[1] C. Li et al., "3-D shear wave velocity structure in the shallow crust of the Tanlu fault zone in Lujiang, Anhui, and adjacent areas, and its tectonic implications," *Earth and Planetary Physics*, Vol. 4, No. 2, pp. 1–12, Jan. 2020, https://doi.org/10.26464/epp2020026

[2] X. Shao et al., "3-D isotropic and anisotropic shallow crustal structure on Pingtan Island, Fujian, southeastern coast of China," *Physics of the Earth and Planetary Interiors*, Vol. 310, p. 106620, Jan. 2021, https://doi.org/10.1016/j.pepi.2020.106620

[3] P. Teves-Costa, L. Matias, C. S. Oliveira, and L. A. Mendes-Victor, "Shallow crustal models in the Lisbon area from explosion data using body and surface wave analysis," *Tectonophysics*, Vol. 258, No. 1-4, pp. 171–193, Jun. 1996, https://doi.org/10.1016/0040-1951(95)00194-8

[4] J. Wu et al., "Attenuation characteristics of impact-induced seismic wave in deep tunnels: An in situ investigation based on pendulum impact test," *Journal of Rock Mechanics and Geotechnical Engineering*, Vol. 14, No. 2, pp. 494–504, Apr. 2022, https://doi.org/10.1016/j.jrmge.2021.12.005

[5] K. Yamaoka, T. Kunitomo, K. Miyakawa, K. Kobayashi, and M. Kumazawa, "A trial for monitoring temporal variation of seismic velocity using an ACROSS system," *Island Arc*, Vol. 10, No. 3-4, pp. 336–347, Jul. 2008, https://doi.org/10.1111/j.1440-1738.2001.00332.x

[6] Z. Li, Q. You, S. Ni, T. Hao, H. Wang, and C. Zhuang, "Waveform retrieval and phase identification for seismic data from the CASS experiment," *Pure and Applied Geophysics*, Vol. 170, No. 5, pp. 815–830, Sep. 2012, https://doi.org/10.1007/s00024-012-0585-2

[7] R. Suzuki, K. Yamaoka, S. Tsuji, and T. Watanabe, "Ground water-induced changes in velocities of P and S waves (Vp and Vs) measured using an accurately controlled seismic source," *Earth, Planets and Space*, Vol. 73, No. 1, p. 152, Jul. 2021, https://doi.org/10.1186/s40623-021-01484-3

[8] X. Wang et al., "A method of phase identification for seismic data acquired with the controlled accurate seismic source (CASS)," *Geophysical Journal International*, Vol. 222, No. 1, pp. 54–68, Jul. 2020, https://doi.org/10.1093/gji/ggaa108

[9] C. Song, J. Feng, and S. G. Dai, "The performance of monitoring system of accurately-controlled routinely-operated seismic source in the Dagangshan Reservoir area and its affecting factors," (in Chinese), *Earthquake Research in China*, No. 2, pp. 417–425, 2016.

[10] Y. B. Dong, B. Hu, and R. Yang, "Active monitoring experiment in Chicheng using precision seismic vibrator," (in Chinese), *North China Earthquake Sciences (in Chinese)*, No. 4, pp. 6–13, 2015, https://doi.org/10.3969/j.issn.1003-1375.2015.04.002

[11] Z. Huang, R. Wang, G. Li, and K. Zhang, "Excitation performance enhancement based on optimization of structural parameters of precision-controllable vibrator," *Advances in Mechanical Engineering*, Vol. 13, No. 6, p. 16878, Jun. 2021, https://doi.org/10.1177/16878140211024876

[12] Z. Huang, R. Wang, L. He, M. Fu, and Y. Xi, "Study on energy excitation effect and structure optimization of vibratory vibrator considering captured road," *Advances in Mechanical Engineering*, Vol. 15, No. 7, p. 16878, Jul. 2023, https://doi.org/10.1177/16878132231186014

[13] Q. Zhang et al., "Research on optimal energy transmission optimization method for precision controllable seismic source," (in Chinese), *Earthquake Engineering and Engineering Dynamics (in Chinese)*, Vol. 45, No. 6, pp. 40–49, 2025, https://doi.org/10.13197/j.eeed.2025.0605

[14] G. Li, W. Qi, Z. Huang, Z. Tao, G. Li, and X. Hu, "Modeling of energy transfer and parameter effects on it of a vibrator-ground system," *Advances in Structural Engineering*, Vol. 23, No. 15, pp. 3251–3262, Jun. 2020, https://doi.org/10.1177/1369433220933982

[15] X. Peng, J. Sun, Y. Li, Z. Teng, and L. Hao, "Modeling and analysis of a shear-wave vibrator-ground coupled system dynamics," *International Journal of Mechanical Sciences*, Vol. 289, p. 110064, Mar. 2025, https://doi.org/10.1016/j.ijmecsci.2025.110064

[16] J. Dai, X. Yan, Z.-D. Xu, Q.-X. Shi, and Y.-Q. Guo, "Active control of earthquake-excited structure using a torsional servomotor active mass driver system," *Structures*, Vol. 61, p. 106011, Mar. 2024, https://doi.org/10.1016/j.istruc.2024.106011

[17] L. Hong, J. Liu, Q. Zhang, and B. Zhang, "Disturbance compensation control method for improving waveform accuracy of controlled active seismic source," *Measurement Science and Technology*, Vol. 36, No. 5, p. 056212, May 2025, https://doi.org/10.1088/1361-6501/add488

[18] R. Noorlandt, G. Drijkoningen, J. Dams, and R. Jenneskens, "A seismic vertical vibrator driven by linear synchronous motors," *Geophysics*, Vol. 80, No. 2, pp. EN57–EN67, Mar. 2015, https://doi.org/10.1190/geo2014-0295.1

[19] X. Ma et al., "Phase identification with VMD and HT combined method for an active seismic source experiment," *Measurement*, Vol. 201, p. 111689, Sep. 2022, https://doi.org/10.1016/j.measurement.2022.111689

[20] T. Ise, T. Torii, N. Morita, S. Togo, and M. Okano, "Hydrostatic asymmetric journal gas bearings for largely unbalanced rotors of seismic ACROSS transmitters," *Journal of Advanced Mechanical Design, Systems, and Manufacturing*, Vol. 1, No. 1, pp. 93–101, Jan. 2007, https://doi.org/10.1299/jamdsm.1.93

[21] B. Feizi and M. Ala Saadeghvaziri, "Optimal design of eccentricity for seismic applications," *Engineering Structures*, Vol. 59, pp. 646–653, Feb. 2014, https://doi.org/10.1016/j.engstruct.2013.11.023

[22] T.-M. Shin and B.-C. Lee, "Seismic response effect on base-isolated rigid structures by mass eccentricity in nuclear plants," *Applied Sciences*, Vol. 13, No. 24, p. 13330, Dec. 2023, https://doi.org/10.3390/app132413330

[23] J. Gao, X. Xing, and J. Zheng, "Optimization of the vibroseis to enhance signal-to-noise ratio for seismic exploration," *IEEE Transactions on Instrumentation and Measurement*, Vol. 74, pp. 1–13, Jan. 2025, https://doi.org/10.1109/tim.2025.3533625

[24] J.-H. Park, P. Sun, J.-H. Kwon, and S.-M. Hwang, "Optimal design of linear vibrators used in touch screen mobile phones," *Journal of Mechanical Science and Technology*, Vol. 27, No. 2, pp. 313–318, Mar. 2013, https://doi.org/10.1007/s12206-012-1247-0

[25] Y. Iwata, T. Komatsuzaki, S. Kitayama, and T. Takasaki, "Study on optimal impact damper using collision of vibrators," *Journal of Sound and Vibration*, Vol. 361, pp. 66–77, Jan. 2016, https://doi.org/10.1016/j.jsv.2015.09.036

[26] Q. Zhang, S. Li, and J. Guo, "Smooth time-optimal tool trajectory generation for CNC manufacturing systems," *Journal of Manufacturing Systems*, Vol. 31, No. 3, pp. 280–287, Jul. 2012, https://doi.org/10.1016/j.jmsy.2012.06.001

[27] Q. Zhang, S. Li, and J. Guo, "Minimum time trajectory optimization of CNC machining with tracking error constraints," *Abstract and Applied Analysis*, Vol. 2014, No. 1, pp. 1–15, Jan. 2014, https://doi.org/10.1155/2014/835098

[28] A. Ademola-Idowu and B. Zhang, "Optimal design of virtual inertia and damping coefficients for virtual synchronous machines," in *2018 IEEE Power and Energy Society General Meeting (PESGM)*, pp. 1–5, Aug. 2018, https://doi.org/10.1109/pesgm.2018.8586187

[29] E. Serea and C. Donciu, "Shaking table design for testing earthquake early warning systems," *Designs*, Vol. 7, No. 3, p. 72, May 2023, https://doi.org/10.3390/designs7030072

[30] Y. Huang, M. Deng, F. Yao, W. Luo, and L. Zhao, "Effects of microscopic properties and calibration on the mechanical behavior of cohesive soil-rock mixtures based on discrete element method," *Applied Sciences*, Vol. 15, No. 19, p. 10529, Sep. 2025, https://doi.org/10.3390/app151910529

[31] H. Pandey, N. K. Gupta, and S. K. Ghosh, "Thermo-structural optimization of air-cooling battery thermoregulation system using surrogate modelling and NSGA-II," *Thermal Science and Engineering Progress*, Vol. 59, p. 103270, Mar. 2025, https://doi.org/10.1016/j.tsep.2025.103270

[32] X. Wu, Z. Chen, T. Liu, H. Song, Z. Wang, and W. Shi, "Improved NSGA-II and its application in BIW structure optimization," *Advances in Mechanical Engineering*, Vol. 15, No. 2, p. 16878, Feb. 2023, https://doi.org/10.1177/16878132221150588

Li Hong is a Professor at the University of Emergency Management. He received the Ph.D. degree in Control Theory and Control Engineering from China University of Petroleum. His research interests include disaster monitoring technologies, seismic observation and intelligent information processing, and emergency management equipment.

Kewen Tian is currently a postgraduate student at the University of Emergency Management. His research focuses on optimal structural design and maximum energy transmission of vibration exciters.

Qiang Zhang received the Ph.D. degree in Control Theory and Control Engineering in 2014 from China University of Petroleum (East China). From 2014 to 2016, he was a postdoctoral researcher at the Academy of Mathematics and Systems Science, Chinese Academy of Sciences. He is currently with the University of Emergency Management. His research interests include vibration excitation systems, active seismic sources, structural optimization, and precision digital control.

Ning Chen received the B.S. degree in Network Engineering from the University of Emergency Management in 2017. She is currently a laboratory instructor at the same institution. Her research interests include seismic instrumentation and the design of engineering vibration measurement instruments.

Yize Liu is an undergraduate student at the University of Emergency Management. His research focuses on optimization methods for seismic source mechanical equipment and related vibration systems.

ISSN PRINT 1392-8716, ISSN ONLINE 2538-8460